University of Dundee

Numerical modelling of rock anchor uplift capacity for offshore applications

Cerfontaine, Benjamin; Brown, Michael; Caton, Adam; Hunt, Andy; Cresswell, Nick

Numerical modelling of rock anchor uplift capacity for offshore applications

B. Cerfontaine, M.J. Brown, A. Caton, A. Hunt and N. Cresswell

Abstract— **Mooring and anchoring represent a significant part of the cost of wave energy converter (WEC) systems. The most common offshore embedded anchor solutions are inapplicable to rocky seabeds, which are likely in zones of strong currents/waves of interest for WECs. A new type of anchor was recently proposed for hard seabeds. It is composed a self-drilling head, which leads the anchor shaft into the rocky seabed. The anchor is then mechanically locked into the rock by applying a pre-tension. This work investigates the rock failure mechanism around the anchor, while subjected to uplift (axial) loading, and for which few models exist. Limit analysis was undertaken to calculate the failure load of the anchor in different configurations (3 rock types, varying depths and anchor geometries). The results indicate that the anchor capacity increases with depth until a certain limit is reached, corresponding to the creation of a local failure mechanism around the anchor, while a wedge failure type takes place at shallower depth. The underreamed contact area must be carefully controlled to maximise the uplift capacity related to the local failure mechanism.**

Keywords—**Anchor, Foundation, Rock.**

I. INTRODUCTION

THE large potential of offshore wave and tidal energy has attracted a lot of attention, with most of research focus placed on the development of efficient wave and tidal energy converters [1]. Many solutions are based on floating device technology, which unlocks deep water locations, reduces the foundation cost, simplifies maintenance and decommissioning. Different mooring systems exist to maintain floating devices in position [2].

Catenary moorings, using long and heavy chains, are widespread in the offshore industry. However, there is a tendency to overdesign these chains, hence impeding cost-effectiveness. The use of intelligent mooring systems [3], introducing non-linear stiffness characteristics by using polymer ropes is a way of reducing mooring tension and cost. The deployment of wave energy converters in arrays [4] is another way of reducing installation and maintenance costs.

In all cases, anchors must be installed to fix the mooring lines into the seabed [5]. Gravity anchors are very inefficient and costly, as heavy lifts or large volumes of material are necessary. Drag embedment anchors [6], suction embedded plate anchors [7], suction caissons [8] or screw piles [9] can be used as anchors in soft soils such as clay or sand. They can mobilise the seabed strength to improve the anchor capacity beyond its own weight. However, all these anchors cannot be embedded into rocky seabeds, which are likely in zones of strong currents and high waves.

Rock anchors are widely used in civil engineering applications (e.g. tunnelling) [11], but a large majority of those anchors are sealed by grouting. In this case, failure almost always takes place in the grouting or at the interface between the grouting and the anchor. Few analytical models estimate the anchor pull-out capacity in the rock itself (described in section II), but scarce experimental evidence exists to validate those approaches.

A new type of marine rock anchor was recently developed by Sustainable Marine Energy (SME) to suit tidal energy requirements [10]. The anchor is composed of a drilling head, a shaft and an upper part with a padeye (see Figure 1) to attach the mooring line. The anchor is mounted on a remotely operated vehicle (ROV) which provides the necessary torque to drill a borehole to the required depth. The anchor is then pre-tensioned by moving the drilling head upwards. This underreams the

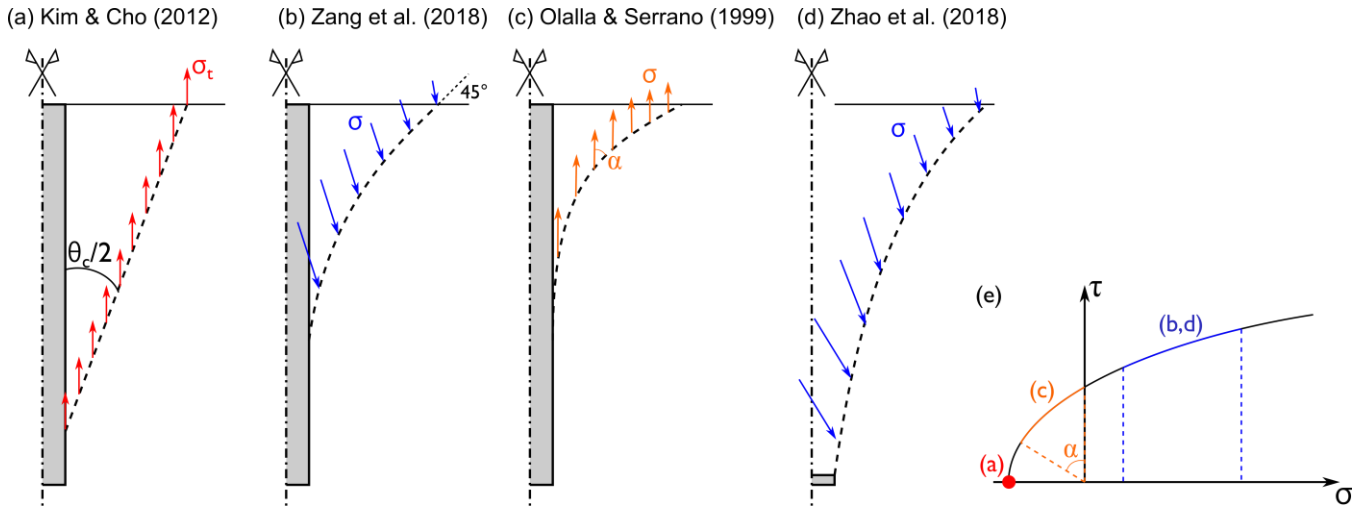Figure 1 View of a self-drilling anchor (rotated of 90°)

Figure 2 (a-d) Failure surfaces and stress distribution at failure for four analytical models; (e) Stress state at failure along the Hoek-Brown failure envelope for each model. The angle of the cone in (a) is denoted θ_c, the tensile strength is σ_t, the (non-tensile) stress state at failure is σ and α is the angle between the stress state and the failure surface.

tip of the anchor by expanding the shaft laterally. The anchor is mechanically locked into the rock and no grouting is necessary, which enables its further decommissioning and potential reuse.

The objective of this paper is to investigate the uplift capacity of mechanically locked rock anchors. Limit analysis will be undertaken to identify their failure mechanism and stress state at failure. The anchor uplift capacity evolution will be shown for different geometries (depth, anchor height) and rock conditions (chalk, sandstone, basalt).

II.   ANALYTICAL MODELS

Only a handful of simplified analytical or semi-analytical models exist to calculate the uplift capacity of rock anchors if the failure takes place in the rock. These methods originate from the design of grouted rock anchors, for which failure will mostly take place in the grouting or at the anchor-grouting interface [11]. Therefore, a very accurate method to estimate the anchor capacity related to failure in the rock is rarely relevant.

There are significant differences between those methods that can be found in the literature to calculate the mechanism geometry and stress distribution at failure, although all consider a Hoek-Brown failure envelope. Figure 2a-d depicts four previous studies with their associated stress state along the failure envelope [12] (Figure 2e).

The criterion proposed by Kim & Cho and based on previous studies [13], [14] (Figure 2a) assumes a conical failure mechanism and considers the rock tensile strength is mobilised all along it at failure. The opening of the cone is usually assumed equal to 90°, as used in practice for a competent rock mass [15]. It must be pointed out that there is no guidance on the evolution of this cone shape as a function of the nature or quality of the rock mass. This approach seems flawed as the hypothesis of mobilising the tensile strength σ_t corresponds to a mode I

(or pure tensile) crack opening as defined in fracture mechanics. According to fracture mechanics theory, the stress mobilised should be orthogonal to the crack propagation direction, as well as the relative velocity between the two moving parts. This does not correspond to the actual relative movement along the failure plane.

The criteria introduced by Serrano & Olalla [16] and Zhang et al. [17] both consider curved failure mechanisms, but different stress distributions: mainly in tension for the former ($\sigma_3 \leq 0$, where σ_3 is the minor principal stress) and mainly in compression ($\sigma_3 \geq 0$) for the latter ($\sigma_3 > 0$, due to the self-weight of rock overburden).

Finally, a single failure mechanism was specifically developed for plate anchors and was proposed by Zhao et al. [18]. It considers a curved failure mechanism, but the stress distribution at failure was not clearly stated. However, it is likely to be mainly in compression. In addition, the method, as proposed by Zhao et al., is not fully defined and the results cannot be replicated easily, because details of the method are missing.

The lack of consensus on failure mechanism and stress state at failure makes the extrapolation of existing models to offshore rock anchors hazardous. The relative complexity of the geometry and rock behaviour makes the use of numerical modelling more suitable to estimate the anchor uplift capacity.

III.   NUMERICAL MODEL

A. Limit analysis

Optum G2 software [19] is a commercial finite element program that was selected for its robustness and its ability to calculate lower and upper bound solutions. Limit analysis enables the identification of the ultimate load multiplier, but also of the failure mechanism and stress state. The software incorporates an automated strategy of mesh adaptivity. The mesh will be refined in

areas where the shear energy dissipation is the largest, namely where shear bands are forming.
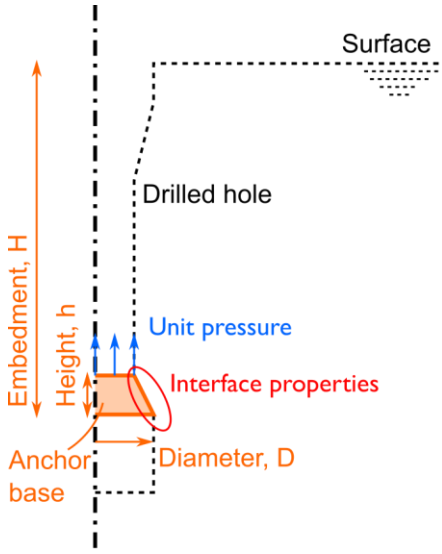

Figure 4 Anchor geometry

B. Model geometry

The anchor geometry is depicted in Figure 4 and is representative of the self-drilling anchor developed by Sustainable Marine Energy [10]. The model geometry was considered axisymmetric as only the vertical (coaxial) capacity was simulated. The drilled hole is enlarged at the bottom (under-reamed, base diameter D) to provide the vertical capacity. The drilled shaft is also enlarged at the top to provide a larger lateral capacity and reaction for the pre-tension. The axisymmetric conditions assume implicitly that there is no preferential pattern of cracks or fractures in the surrounding rock. The anchor dimensions are confidential, and results will be shown in the following in a non-dimensional manner.

Boundary conditions are assumed to be normally fixed along all boundaries except at the top surface. There is theoretically no need of manual mesh refinement as the software automatically adapts the mesh based on the dissipated shear energy. However, the mesh was refined close to the anchor to allow the 'initiation' of shear bands in this area. A maximum number of 3000 elements were used (see section IV.A) and three adaptive iterations were selected.

Shear joints were used between the rigid anchor and the rock mass to simulate the steel-rock interface.

C. Hoek-Brown constitutive model

The Hoek-Brown failure envelope is widely used for design [12]. The generalised model for rock masses is defined in the two principal stresses (σ_1, σ_2), positive in compression
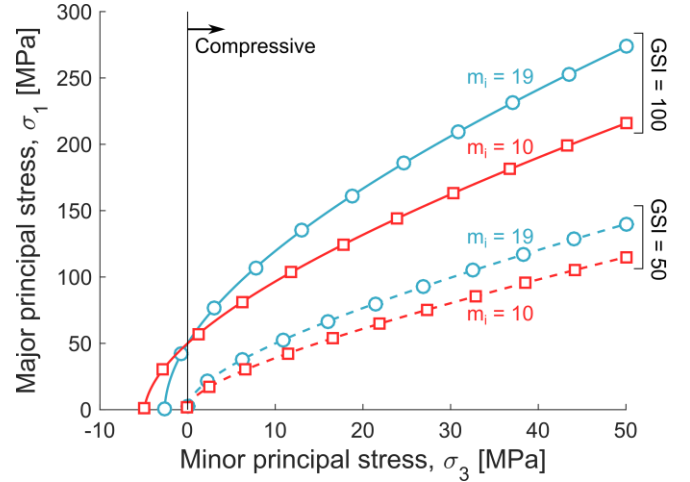

Figure 3 Hoek and Brown failure criterion in principal stress space, $\sigma_c = 50$MPa, varying m_i and GSI.

$$\sigma_1 = \sigma_3 + \sigma_c \left(m_b \frac{\sigma_3}{\sigma_c} + s \right)^a \qquad (1)$$

where σ_c is the unconfined uniaxial strength of the intact rock and the other parameters are calculated according to

$$m_b = m_i \exp\left[\frac{GSI - 100}{28 - 14D} \right] \qquad (2)$$

$$s = \exp\left[\frac{GSI - 100}{9 - 3D} \right] \qquad (3)$$

$$a = \frac{1}{2} + \frac{1}{6}\left(\exp\left[-\frac{GSI}{15} \right] - \exp\left[-\frac{20}{3} \right] \right) \qquad (4)$$

where m_i is a material parameter describing the curvature of the Hoek-Brown model, D is the disturbance resulting from installation process (assumed equal to zero here) and the GSI is the Geological Strength Index, which empirically assesses the rock mass properties, from the intact rock parameters and on-site observations [12].

An example of the failure criterion is shown in Figure 3 for $\sigma_c = 50$MPa and two values of m_i (10 or 19) and GSI (100 or 50). Changing the m_i parameter, modifies the overall shape of the failure criterion, with lower compressive and greater tensile strengths as a function of σ_3 (at constant unconfined strength when $\sigma_3 = 0$MPa).

TABLE I
MATERIAL PARAMETERS USED FOR THE SIMULATIONS

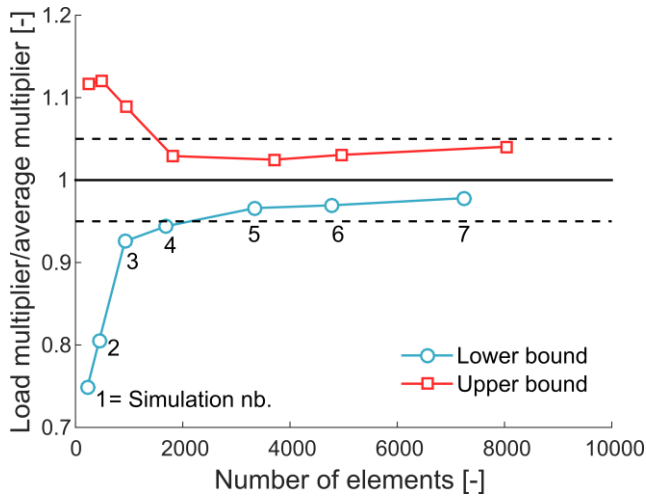| Symbol	Unit	Chalk	Sandstone	Basalt
σ_c	MPa	2.5	50	150
m_i	-	7	17	19
E	GPa	2.5	13.75	52.5
δ	°	12	12	12
ν	-	0.2	0.2	0.2
γ_{rock}	kN/m³	29	29	29

Figure 5 Convergence of lower bound and upper bound solutions.

Reducing the GSI affects the whole shape of the failure criterion and 'scales it down', to reproduce the strength of the whole rock mass, which contains blocks of intact rock and discontinuities.

The underlying hypothesis behind the Hoek-Brown model is that the failure process is dominated by block sliding and rotation without a great deal of intact rock failure, under low to moderate confining stresses [12], [20]. Therefore, the rock mass can be modelled as a continuum, which also requires that the size of the modelled structure is large with respect to the size of the rock blocks. The original Hoek-Brown model is also valid for intact rocks (GSI = 100), but if the size of rock blocks is equivalent to the structure size, discontinuities should be modelled explicitly [12]. In the following, different values of the GSI are considered and it is assumed that the model hypotheses are valid in all cases.

Three rock types have been considered in the following, representative of a range of rock types: a basalt, a chalk (selected to obtain a very weak rock) and a sandstone. Intact properties of these materials can be found in Table I. These material properties do not correspond to a specific site and have been chosen as average values based on the literature ([21], [22]). Young's modulus (E_i) and Poisson's ratio (ν) were provided for completeness, although they are not necessary for the limit analysis. The plastic potential of the rock behaviour is deemed associated, as assumed by all analytical methods presented before. There is no cap surface in compression (no crushing limit). Finally, the rock mass was assumed dry for simplicity (unit weight, γ_{rock} = 29kN/m³).

The interface friction angle varies as a function of the rock type, the relative roughness and the normal stress as reported in Ziogos et al. [23]. However, it was initially selected equal to 12° in all cases to simplify the problem.

IV. RESULTS

A. Lower and upper bound solutions

The first step consists in assessing the number of elements necessary to accurately capture the failure mechanism of the anchor upon axial tensile load. The lower and upper bound failure multipliers were calculated for an anchor embedded at H/D = 4 in basalt, as a function of the number of elements considered. Results of seven simulations are depicted in Figure 5 and are normalised with the average multiplier for the largest number of elements. This figure shows that a relatively low number of elements is sufficient (simulation nb. 5, ≥ 3000) to reach a fairly accurate result, for which both lower and upper bound solutions are within ±5% of the average value. The resulting meshes after the adaptive refinement are depicted in Figure 6. This figure shows the high density of elements in a zone extending from the anchor to the surface, indicating that the failure mechanism at this depth is a conical wedge. In the following, the same mesh density as in simulation nb. 5 will be applied to all simulations and only lower bound solutions will be depicted.

B. Failure mechanism

The shear strain corresponding to Figure 6(b) was further analysed in Figure 7(a). This figure shows that the shear strain is the highest where the mesh was the most refined, which was expected. This high shear strain (γ) defines the active failure mechanism and is shown to be slightly non-linear. It also seems to show a point of inflection in the mechanism geometry, which will be used to distinguish between a near-field and a far-field.

Several points were manually selected along the mechanism, and the principal stress state (σ_1, σ_2) was extracted. The selected points correspond to integration

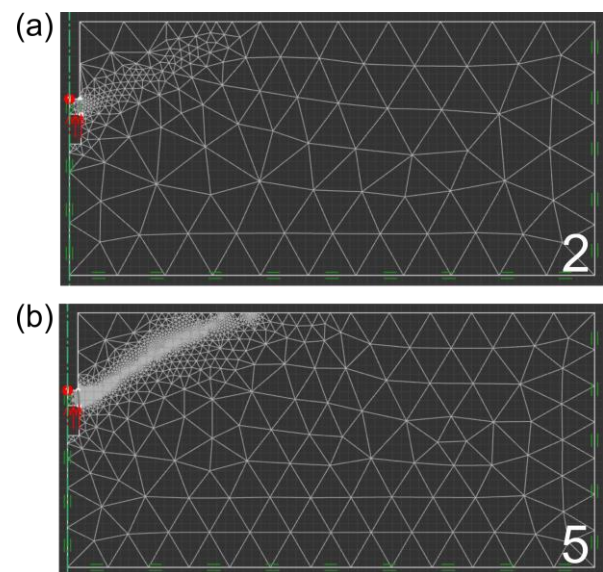

Figure 6 Meshes for simulations nb. 2 and 5, H/D = 4, basalt rock

points of the elements. The spacing between the points increases with radial distance as less stress variation is expected further from the anchor. The principal stresses along the failure mechanism are depicted as a function of the radial distance from the axis of symmetry in Figure 7 (b). This figure shows that the stress magnitude is far from constant along the failure surface. The stress magnitude is high close to the anchor, but fast decreases with the radial distance. This can be explained by the load transfer from the anchor to the rock, which induces high stress magnitude close to the anchor. This in turn increases the normal stress along the failure mechanism, hence the shear stress that can be mobilised.

The stress state is compared with the Hoek-Brown envelope in Figure 7 (c). This figure shows that failure was reached at all these points, but also that the existing minor principal stress varies from tensile to compressive. This means that none of the previously described analytical model hypotheses (see section II) are correct for the anchor loading presented herein.
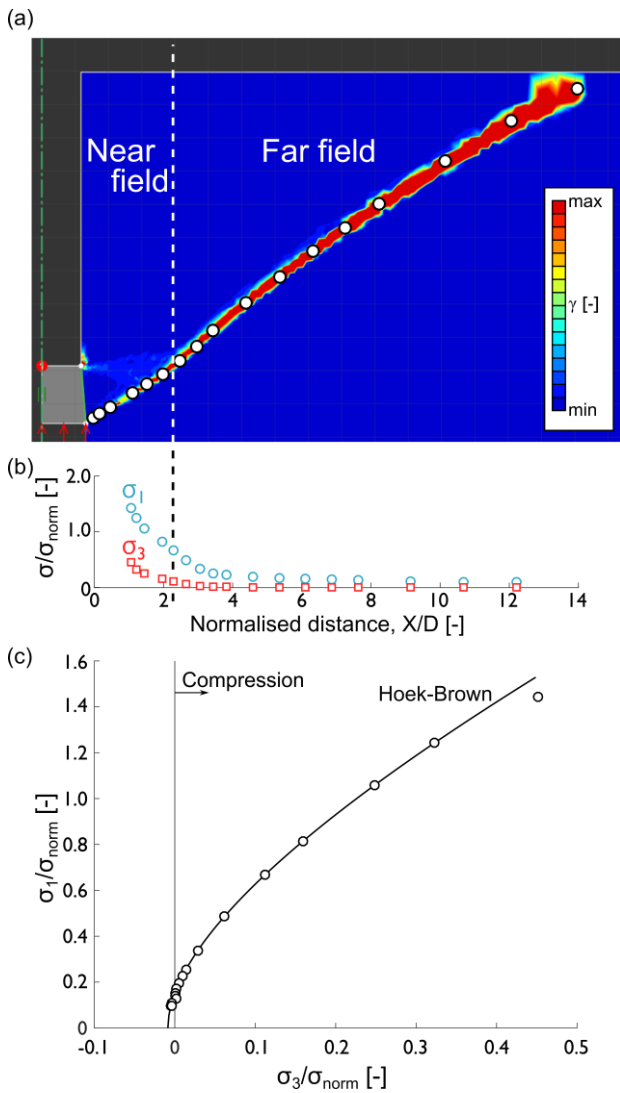

Figure 7 (a) Shear strain and (b) normalised stress state at failure as a function of radial distance; (c) Comparison of the stress state with the Hoek-Brown failure envelope. H/D = 4, basalt rock.
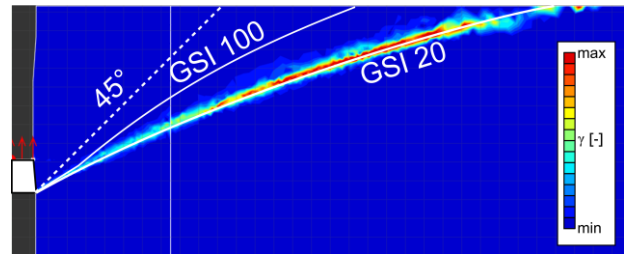

Figure 8 Shear strain at failure as a function of the GSI, H/D = 4, basalt rock. The shape of the mechanism for GSI = 100 is depicted by a solid white line.
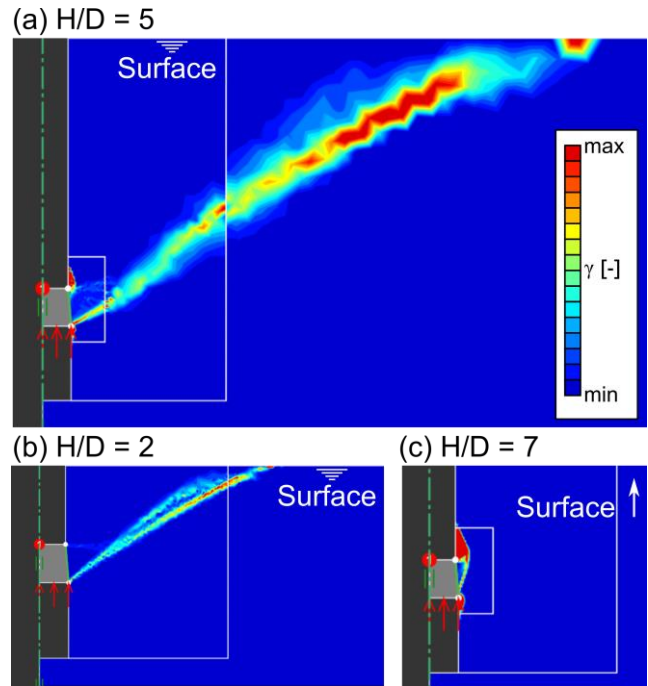

Figure 9 Shear strain at failure as a function of the relative embedment depth. Subfigure (c) was cropped for space, therefore the top of the figure is not the rock surface.

The GSI was varied between 20 and 100 for the same basalt intact rock parameters and anchor embedment depth (H/D=4). Figure 8 shows how the failure mechanism varied in shape, with a widening of the uplifted rock wedge with a decreasing GSI. In both cases, the size of the wedge was wider than a 90° opening conical shape, as assumed in some of the analytical models.

C. Depth effect

Depth is often one of the main parameters controlling anchor capacity, e.g. for plate anchors [24]. Therefore, the depth of the anchor was progressively increased and the load multiplier was collected at the end of each simulation. This was repeated for three sets of parameters corresponding to different rock types (weak chalk, sandstone and basalt), whose GSI was also varied between, 20 and 100.

Figure 10 summarises all the results, for which the uplift capacity was normalised by the uplift capacity calculated in chalk at the maximum GSI (100) and embedment depth (H/D =8). In all cases, the uplift
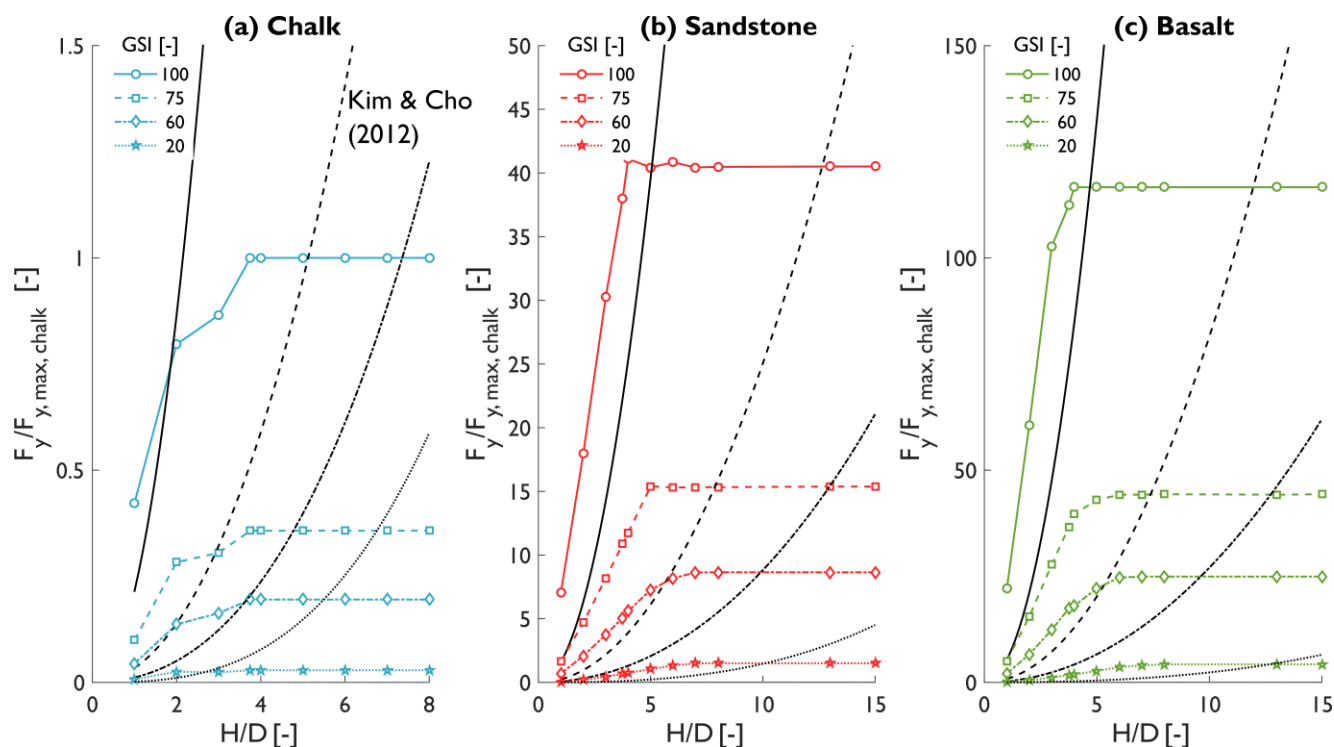
Figure 10 Comparison of the normalised uplift capacity of the anchor as a function of the relative embedment depth, GSI and rock type: (a) Chalk; (b) Sandstone; (c) Basalt. The black lines represent the Kim & Cho (2012) criterion for each GSI.

capacity follows the same pattern with increasing depth. First the anchor capacity increases almost linearly with depth, then it reaches a plateau and remains constant even at deeper embedment. This is due to a change in the failure mechanism, as depicted by the shear strain at failure in Figure 9 in basalt rock. At very shallow embedment depth, the failure surface is almost a linear cone (Figure 9b). At intermediate depth, the failure surface becomes non-linear (Figure 9a) but still reaches the surface. Beyond a critical embedment depth, a local failure mechanism develops around the anchor (Figure 9c). Whilst the failure mechanism is shallow, additional resistance can be mobilised with a greater depth, hence a greater cone volume and surface. However, when the local failure mechanism is reached, no extra capacity can be mobilised by increasing depth. The maximum capacity is strongly reduced with the GSI, which makes sense as the GSI directly affects the rock mass strength. Reducing the GSI also changes the relative embedment depth at which there is a transition from a shallow wedge mode of failure to a deeper local mode of failure.

Finally, the numerical results were compared with the closed-form analytical solution of Kim & Cho [13] for each rock type and GSI. This solution underpredicts the anchor capacity at low embedment depth, but largely overpredicts their capacity at deeper depths, when the local failure mechanism takes place.

D. Local failure mechanism

It was shown in the previous section that capturing the local failure mechanism is critical to design the rock anchor. If the depth necessary to reach the deep local

mechanism is achieved, there is no economic gain in installing it deeper. However, the anchor capacity associated with the local failure mechanism must not be overestimated.

A slightly different anchor was tested to assess how the local mechanism is dependent on the anchor geometry. A shorter anchor underreamed part was tested (h is 60% of the original value) with a slightly steeper inclination of the lateral face.

Normalised results are depicted in Figure 11, together with the previous ones (from Figure 10). This figure shows that anchors with a reduced height have a lower maximum capacity (plateau in Figure 11), although the initial increase in capacity with depth (initial slope in Figure 11) is identical for both anchor geometries. This suggests that the shallow failure mechanism (rock wedge) is relatively insensitive to the anchor shape, as failure takes place relatively far away from the anchor. On the other hand, the local deep failure mechanism is highly dependent on the anchor geometry. Additional results, not depicted here, also showed that increasing the steel-rock interface friction angle increased the capacity of the anchor at a given depth and modifies the shallow-deep mechanism transition depth.

E. Discussion

The local failure mechanism can be idealised as shown in Figure 12. A small volume of material adjacent to the anchor detaches from the rock mass and moves towards the centre of the borehole. The failure mechanism initiates at the anchor lower edge (point A in Figure 12) and extends radially (to point D) before curving back to the
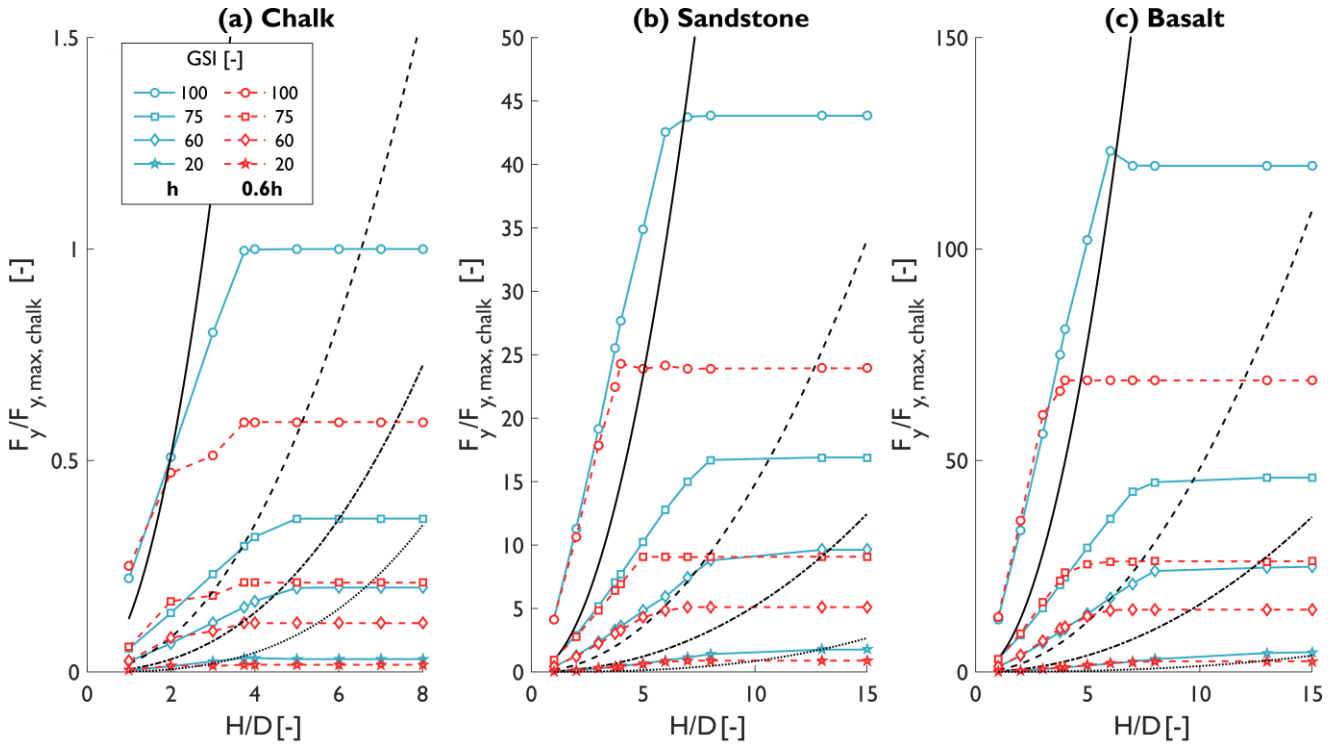
Figure 11 Comparison of the normalised uplift capacity of the anchor as a function of the relative embedment depth, GSI and rock type, for two anchor heights (original h, reduced 60% h): (a) Chalk; (b) Sandstone; (c) Basalt

borehole (point C). The failure mechanism is somewhat similar to a reverse slope failure mechanism, but in axisymmetric conditions.

The stress state along steel-rock interface (A-B) can be considered at failure, as the interface friction angle is lower than the rock friction angle. The normal stress magnitude along A-B is high and induces large high stress magnitude along A-D, as the rock block horizontal equilibrium must be maintained. Therefore, the shear stress magnitude that can be mobilised in this zone is high. Along C-D, the normal stress magnitude is much lower, and a part of the stress state can be on the tensile side ($\sigma_n < 0$). Finally, it was assumed that the shaft was not in contact with the rock along B-C, and there is no stress applied along this boundary.
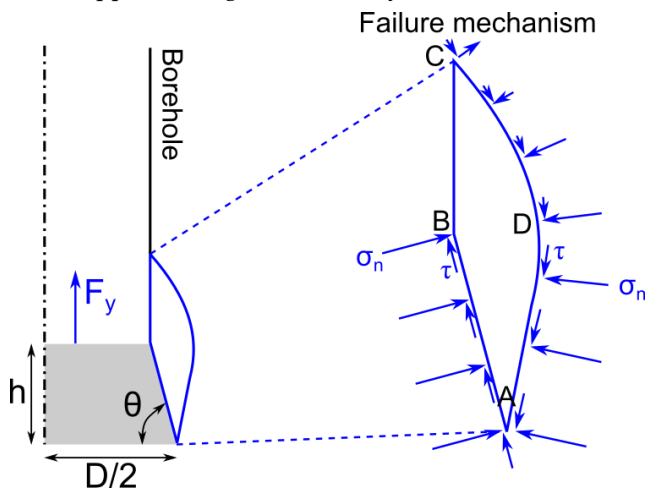

Figure 12 Idealisation of the local failure mechanism

Based on this simplified theoretical model, it is obvious how important the contact area is (A-B in Figure 12). Increases in the lateral face inclination or reduction in its height will both modify the size of the failure mechanism and stress state at failure. It is clear that the mechanical locking part of the anchor installation process must be done cautiously and the prediction of the achieved contact area is critical in the design process.

Three potentially important phenomena have not been included in this study. Firstly, there is no crushing limit for the rock and the only possible failure is a shear failure. This could affect the local failure mechanism, as the high stress state in this area could reach a crushing limit, especially for some more porous rocks such as chalk. This could be verified by undertaking a finite element simulation and verifying that the average stress in the contact area is lower than the crushing limit. Secondly, the shaft was not included in the simulation, because there must be a technical gap during installation, which enables the movement of the rock block. If the technical gap was filled with some extra material, it could impede or modify the shape of the local failure mechanism. Finally, the potential for progressive crack propagation in an initially intact rock could lead to a lower capacity.

V. CONCLUSION

Limit analysis modelling of the failure mechanism created by the uplift of mechanically locked rock anchors was undertaken in this work. The simulations highlighted that two failure mechanisms must be considered for design, one shallow (almost conical

wedge) and one deep (local around the anchor). The anchor capacity increases with depth, until a critical depth is reached and the local failure mechanism develops. The failure load associated with the local failure mechanism depends on the contact area, lateral face inclination and interface friction angle. None of these parameters or local failure mechanism were included into existing analytical or semi-analytical models.

The results presented here can be used to develop new analytical or semi-analytical methods to enable a fast and accurate design of new anchors for offshore energy applications. The shape and stress state at failure can be directly identified, which should facilitate the choice of analytical models. Future work will focus on the combination of lateral and vertical loading, as well as cyclic loading of the anchor to represent more realistic loading conditions.

ACKNOWLEDGEMENT

REFERENCES

[1]   H. P. Nguyen, C. M. Wang, Z. Y. Tay, and V. H. Luong, "Wave energy converter and large floating platform integration: A review," *Ocean Eng.*, vol. 213, no. February, p. 107768, 2020, doi: 10.1016/j.oceaneng.2020.107768.

[2]   S. Xu, S. Wang, and C. Guedes Soares, "Review of mooring design for floating wave energy converters," *Renew. Sustain. Energy Rev.*, vol. 111, no. March, pp. 595–621, 2019, doi: 10.1016/j.rser.2019.05.027.

[3]   M. J. Harrold, P. R. Thies, D. Newsam, C. B. Ferreira, and L. Johanning, "Large-scale testing of a hydraulic non-linear mooring system for floating offshore wind turbines," *Ocean Eng.*, vol. 206, no. November 2019, p. 107386, 2020, doi: 10.1016/j.oceaneng.2020.107386.

[4]   R. P. F. Gomes, L. M. C. Gato, J. C. C. Henriques, J. C. C. Portillo, B. D. Howey, K. M. Collins, M. R. Hann, and D. M. Greaves, "Compact floating wave energy converters arrays: Mooring loads and survivability through scale physical modelling," *Appl. Energy*, vol. 280, no. May, p. 115982, 2020, doi: 10.1016/j.apenergy.2020.115982.

[5]   J. Knappett, M. Brown, H. Aldaikh, S. Patra, C. O'Loughlin, S. Chow, C. Gaudin, and J. Lieng, "A review of anchor technology for floating renewable energy devices and key design considerations," *Front. Offshore Geotech. III*, no. Richardson 2008, pp. 887–892, 2015, doi: 10.1201/b18442-127.

[6]   C. P. Aubeny and C. Chi, "Mechanics of Drag Embedment Anchors in a Soft Seabed," *J. Geotech. Geoenvironmental Eng.*, vol. 136, no. 1, pp. 57–68, 2010, doi: 10.1061/(asce)gt.1943-5606.0000198.

[7]   Q. Wei, M. J. Cassidy, Y. Tian, and C. Gaudin, "Incorporating Shank Resistance into Prediction of the Keying Behavior of Suction Embedded Plate Anchors," *J. Geotech. Geoenvironmental Eng.*, vol. 141, no. 1, p. 04014080, 2015, doi: 10.1061/(asce)gt.1943-5606.0001193.

[8]   L. Zhao, C. Gaudin, C. D. O'Loughlin, J. P. Hambleton, M. J. Cassidy, and M. Herduin, "Drained capacity of a suction caisson in sand under inclined loading," *J. Geotech. Geoenvironmental Eng.*, vol. 145, no. 2, pp. 1–12, 2019, doi: 10.1061/(ASCE)GT.1943-5606.0001996.

[9]   B. Cerfontaine, J. Knappett, M. J. Brown, C. Davidson, and Y. Sharif, "Optimised design of screw anchors in tension in sand for renewable energy applications," *Ocean Eng.*, vol. 217, 2020, doi: 10.1016/j.oceaneng.2020.108010.

[10]   N. Cresswell, J. Hayman, A. Hunt, and P. Jeffcoate, "Anchor Installation for the Taut Moored Tidal Platform PLAT-O," 2016.

[11]   E. T. Brown, "Rock engineering design of post-tensioned anchors for dams - A review," *J. Rock Mech. Geotech. Eng.*, vol. 7, no. 1, pp. 1–13, 2015, doi: 10.1016/j.jrmge.2014.08.001.

[12]   E. Hoek and E. T. Brown, "The Hoek–Brown failure criterion and GSI – 2018 edition," *J. Rock Mech. Geotech. Eng.*, vol. 11, no. 3, pp. 445–463, 2019, doi: 10.1016/j.jrmge.2018.08.001.

[13]   H. K. Kim and N. J. Cho, "A design method to incur ductile failure of rock anchors subjected to tensile loads," *Electron. J. Geotech. Eng.*, vol. 17 T, pp. 2737–2746, 2012.

[14]   D. F. Coates and Y. S. Yu, "Rock anchor design mechanics," Ottawa, Canada, 1971.

[15]   G. S. Littlejohn and D. A. Bruce, "Rock anchors - Design and quality control." 1975.

[16]   A. Serrano and C. Olalla, "Tensile resistance of rock anchors," *Int. J. Rock Mech. Min. Sci.*, vol. 36, no. 4, pp. 449–474, 1999, doi: 10.1016/S0148-9062(99)00021-2.

[17]   Q. Q. Zhang, R. F. Feng, Z. H. Xu, S. W. Liu, and J. . Qian, "Evaluation of Ultimate Pullout Capacity of Anchor Cables Embedded in Rock Using a Unified Rupture Shape Model," *Geotech. Geol. Eng.*, vol. 0, 2018, doi: 10.1007/s10706-018-00782-0.

[18]   L.-H. Zhao, X.-P. Yang, F. Huang, Y.-G. Tang, and S.-H. Hu, "Variational analysis of the ultimate pullout capacity of shallow circular anchor plates in rock foundations based on the Hoek-Brown failure criterion," *Int. J. Rock Mech. Min. Sci.*, vol. 106, pp. 190–197, 2018, doi: 10.1016/j.ijrmms.2018.04.027.

[19]   K. Krabbenhoft, A. V. Lyamin, and J. Krabbenhoft, "OptumG2: Theory," 2016.

[20]   R. P. Bewick, P. K. Kaiser, and F. Amann, "Strength of massive to moderately jointed hard rock masses," *J. Rock Mech. Geotech. Eng.*, vol. 11, no. 3, pp. 562–575, 2019, doi: 10.1016/j.jrmge.2018.10.003.

[21]   E. Hoek and E. T. Brown, "Practical estimates of rock mass strength," *Int. J. Rock Mech. Min. Sci.*, vol. 34, no. 8, pp. 1165–1186, 1997, doi: 10.1016/S1365-1609(97)80069-X.

[22]   E. Hoek and M. S. Diederichs, "Empirical estimation of rock mass modulus," *Int. J. Rock Mech. Min. Sci.*, vol. 43, no. 2, pp. 203–215, 2006, doi: 10.1016/j.ijrmms.2005.06.005.

[23]   A. Ziogos, M. J. Brown, A. Ivanovic, and N. Morgan, "Chalk – steel interface testing for marine energy foundations," *Proc. Inst. Civ. Eng.*, vol. 170, no. 3, pp. 285–298, 2017.

[24]   B. Cerfontaine, J. A. Knappett, M. J. Brown, and A. S. Bradshaw, "Effect of soil deformability on the failure mechanism of shallow plate or screw anchors in sand," *Comput. Geotech.*, vol. 109, 2019, doi: 10.1016/j.compgeo.2019.01.007.